A DNA recognition code for probing the *in vivo* functions of zinc finger transcription factors at domain resolution

Berat Dogan[1,2,4,¶], Senthilkumar Kailasam[1,2,¶], Aldo Hernández Corchado[1,2], Naghmeh Nikpoor[3], Hamed S. Najafabadi[1,2,*]

[1] McGill University and Genome Quebec Innovation Centre, Montreal, QC, Canada

[2] Department of Human Genetics, McGill University, Montreal, QC, Canada

[3] Rosell Institute for Microbiome and Probiotics, Montreal, QC, Canada

[4] Current address: Department of Biomedical Engineering, Inonu University, Malatya, Turkey

[¶] These authors contributed equally to this work.

* Correspondence should be addressed to: H.S.N., hamed.najafabadi@mcgill.ca

Abstract

Multi-zinc finger proteins are the largest class of human transcription factors, whose DNA-binding specificity is often encoded by a subset of their tandem Cys2His2 zinc finger (ZF) domains. However, the molecular code that underlies ZF-DNA interaction is incompletely understood, and in most cases the ZF subset that is responsible for *in vivo* DNA binding is unknown. We developed a context-aware machine-learning-based model of DNA recognition and combined it with molecular dynamics analyses to uncover new structural aspects of ZF-DNA interaction, including novel residues that contribute to sequence specificity. By combining this model with *in vivo* binding data, we identified the sequence preference and the ZF subset that is responsible for DNA binding in ~30% of all human multi-ZF proteins, showing that *in vivo* DNA binding is primarily driven by ~50% of the ZFs. Analysis of genetic variation within and across species showed that DNA-binding ZFs are under strong selective pressure, and a pan-cancer analysis across 18 tissues revealed hundreds of genes whose expression is affected by somatic coding mutations in DNA-binding ZFs. Together, these results suggest that the regulatory consequences of mutations in ZFs depend on their *in vivo* DNA-binding functionality, which in turn is determined by a combination of context as well as ZF-intrinsic features.

Introduction

Cys2His2 zinc finger proteins (C2H2-ZFPs) make up the largest class of human transcription factors (TFs): the human genome encodes ~750 C2H2-ZFPs, which constitutes ~45% of all human TFs. Most C2H2-ZFPs recognize distinct DNA sequences, which form the most diverse regulatory lexicon of all human TFs[1]. These proteins are characterized by the presence of multiple DNA-binding domains known as Cys2His2 zinc fingers (ZFs). Each ZF typically interacts with three to four nucleotides[2], and the amino acid-base interactions of consecutive ZFs determine the overall DNA sequence specificity of each C2H2-ZFP.

The molecular principles that dictate the relationship between the amino acid sequence of ZFs and their preference for specific DNA sequences have been studied for decades. Earlier studies mostly focused on the 3D structure of a few C2H2-ZFPs[3] and a limited number of mutation analyses[4] to derive simple models of DNA recognition by ZFs, highlighting the role of four "specificity residues" in determining the binding preference (**Fig. 1a**). Extensive *in vitro* binding data from thousands of ZFs has enabled recent studies to generate more complex "recognition codes" by correlating the amino acid sequences of the ZFs with their binding preferences[1,5-7]. These machine-learning-based recognition models have enabled the discovery of integral and unexpected roles for C2H2-ZFPs[8] and new insights into their evolution[9,10].

However, these models have substantial limitations; most importantly, they are derived from *in vitro* experiments in which individual ZFs are tested in an unnatural context (e.g. as fusion to ZFs of other proteins[1,6]), disregarding the influence of adjacent ZFs on DNA binding specificity[11]. Furthermore, most recognition models are based on the identity of the four specificity residues, ignoring the potential contribution of other ZF positions. As a result of these limitations, the predictions made by existing recognition codes only partially match the observed *in vivo* preferences of C2H2-ZFPs[1,11].

Understanding the relationship between ZFs and *in vivo* DNA binding has been further complicated by the fact that not all ZFs of a C2H2-ZFP engage with the DNA: The human C2H2-ZFPs on average contain ~10 ZFs[1], which would correspond to a binding footprint of ~30 nucleotides. However, the binding sites of C2H2-ZFPs are often much shorter[12], suggesting that only a fraction of the ZFs interact with the DNA while other ZFs might be involved in other functions such as mediating protein-protein[13] or protein-RNA[14] interactions. Currently, the DNA-engaging ZFs of only a small subset of C2H2-ZFPs have been characterized[15-17], preventing a comprehensive functional stratification of ZFs.

Here, we take advantage of a large set of recently published *in vivo* C2H2-ZFP binding preferences[18,19] and combine them with *in vitro* data[1] to derive a recognition code of ZF-DNA interaction that is significantly more accurate than existing models. We show that this code captures the contribution of non-canonical ZF residues as well as adjacent ZFs to DNA binding preference, and provides an amino acid-resolution map of ZF-DNA interaction. Furthermore, by combining this recognition code with ChIP-seq and ChIP-exo binding data, we identify the ZF domains that engage with DNA *in vivo*, and examine the evolutionary pressures acting on these DNA-engaging ZFs across species and across individuals in the human population.

Results

Base-specificity of C2H2-ZF proteins is not limited to canonical contact residues

The canonical model of C2H2-ZF interaction with DNA primarily includes four "specificity residues", each of which interacts with four specific sites on the DNA. However, this model is obtained from a limited number of protein-DNA complex structures, mutation experiments, and *in vitro* data. In order to examine whether other ZF residues might contribute to sequence-specificity, we correlated the protein sequence of 836 ZF domains from 157 human C2H2-ZF proteins with their *in vivo* binding preferences. Specifically, we used ChIP-seq and ChIP-exo data from two previously published large-scale datasets[18,19] in order to identify the *in vivo* binding preference of each protein. We then divided the *de novo*-identified motifs into three-nucleotide partitions (triplets) each representing the binding preference of one ZF domain, and examined whether the amino acid identity at each ZF position is informative about the base preference at different positions of the triplet. We observed highly significant dependencies between amino acid identity and DNA base identity for all expected canonical interactions (**Fig. 1b**). However, the significant correlations were not limited to these positions, and included other interactions, e.g. between residue +2 and DNA triplet position +3, and residue +6 and all three DNA triplet positions as well as DNA position +3 of the upstream triplet (**Fig. 1b**).

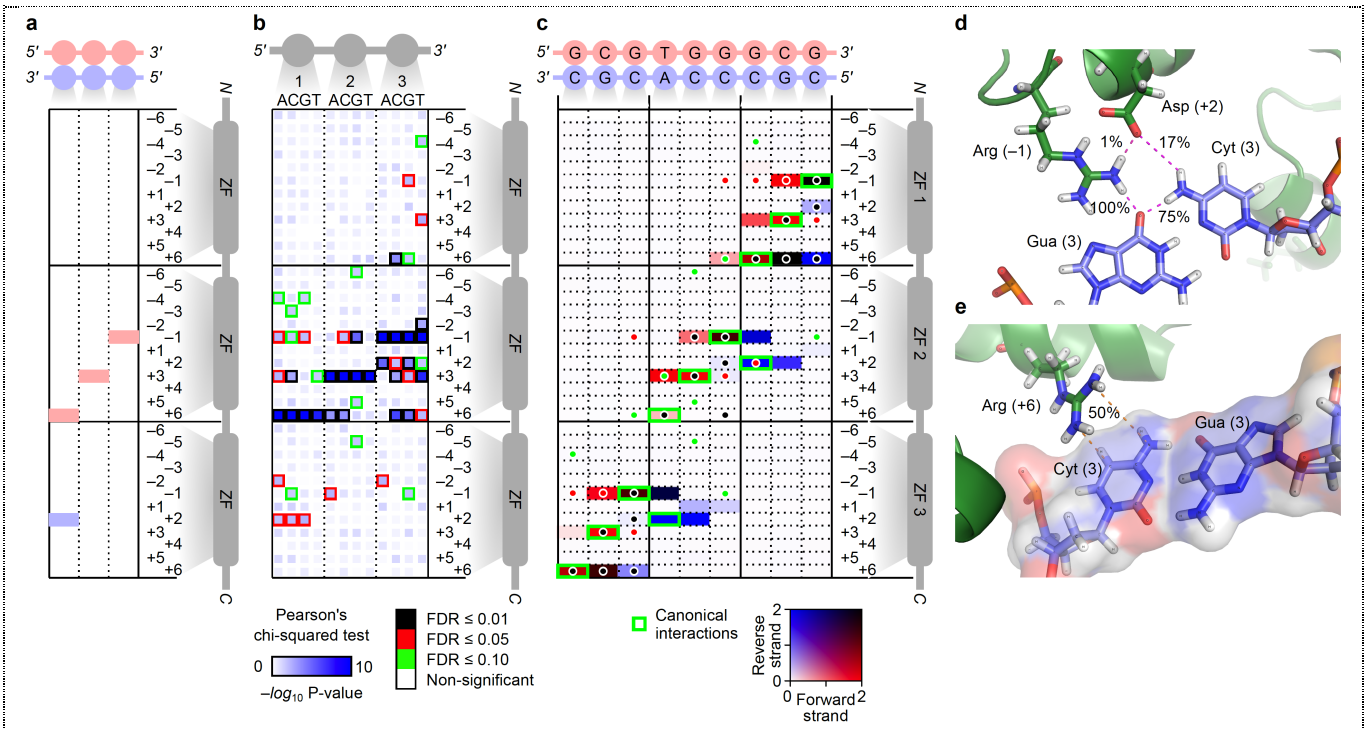

Figure 1. The canonical model of C2H2-DNA interaction only explains a subset of possible contacts. (**a**) Schematic representation of the canonical interactions between ZF positions –1, +2, +3, and +6 with a DNA triplet. Red and blue depict interaction with forward and reverse strand, respectively. Residue numbers are relative to the start of ZF alpha helix. (**b**) Associations between the identity of different ZF residues and each of four bases at different DNA positions, based on *in vivo* motifs. After splitting *in vivo* motifs into triplets, the probability of each base at each triplet position was discretized into two bins, and a chi-square test was used to examine the association of discretized probabilities with amino acid identity at each ZF position, including the N-terminal and C-terminal neighbors of the directly contacting ZF. The color gradient represents the P-value of the test. The border color of the squares represents the level of significance after Benjamini-Hochber correction for multiple hypothesis testing. Data underlying this figure are included in **Table S1**. (**c**) A 1μs-long MD simulation was used to measure the average all-atom contacts between each residue of Egr1 and the nucleotide bases of the forward and reverse strand of the target DNA, based on PDB structure 4X9J. The color gradient stands for the average number of contacts observed per frame of MD simulations, with red and blue representing contact with forward and reverse DNA strands, respectively. The dots represent significant associations based on correlation analysis of *in vivo* binding preferences, with the dot colour mirroring the border colour in panel a. Underlying data are provided in **Table S2**. (**d**) Structural illustration of a non-canonical hydrogen bond between position +2 of Egr1 ZNF1 and the reverse strand base at position 9 of the DNA sequence (i.e. position 3 of the third triplet), which can be observed at ~17% occupancy. (**e**) The planar guanidino group of Arginine in position +6 of ZF1 forms a π-π stacking interaction with reverse strand base of the DNA position 9 (~50% occupancy).

In order to understand whether these non-canonical associations may actually correspond to interactions between ZF residues and target DNA bases, we used molecular dynamics (MD) to track the amino acid-base contacts in the Egr1-DNA complex. Interestingly, many of the correlations observed from *in vivo* binding preferences can be captured as hydrogen bonds and other non-covalent interactions (e.g. van der Waals, ionic, or stacking interactions) in the Egr1-DNA complex (**Fig. 1c**). Example structures highlighting some of these contacts are shown in **Fig. 1d,e**, including a non-canonical hydrogen bond and a π-π stacking interaction between DNA and positions +2 and +6 of ZF1, respectively. Together, these analyses suggest that amino acid-base interactions are not limited to the canonical model, which has also been suggested previously based on analysis of C2H2-ZFP structural data[20]. Given that these associations can be captured using available *in vivo* binding preferences, we set to develop a computational recognition code that takes into account these non-canonical interactions, including the interactions between a DNA triplet and neighboring C2H2-ZFs.

Combining *in vitro* and *in vivo* data results in an improved context-aware recognition code

The *in vivo* binding preferences of C2H2-ZFPs provide the opportunity to capture non-canonical ZF-DNA contacts as well as the effect of neighboring ZFs on DNA sequence recognition. The available *in vitro* data[1], on the other hand, provide a higher coverage and larger training dataset for modeling ZF-DNA interactions.

Therefore, we sought to obtain a "compound recognition code" (hereafter referred to as C-RC), which combines *in vitro* and *in vivo* data in order to obtain optimal prediction accuracy. We performed a systematic feature selection to identify the ZF residues that maximize prediction accuracy when they are used as input to random forest regression models[21] that predict specificity for each of four bases at each DNA triplet position (**Fig. 2a**). We identified different features that optimize prediction accuracy in different contexts – the contexts that we considered included whether the ZF was located at the N-terminus, C-terminus, or the middle of a DNA-engaging ZF-array (**Fig. S1**).

In addition, we also examined whether different encodings of the amino acids can improve prediction accuracy by reducing the number of parameters of the recognition code. Previous attempts at developing a C2H2-ZF recognition code have considered the 20 amino acids as unrelated identities, e.g. through one-hot encoding[1]. However, amino acids with similar biochemical and/or structural properties often have similar propensities for interaction with different bases. Therefore, we specifically examined the possibility that encoding the amino acids by their biochemical properties (**Fig. 2b**) may reduce the complexity of the parameters that our computational model needs to learn, and therefore increase the model accuracy and generalizability. This encoding indeed allowed the random forest to learn simpler rules that were shared among amino acids with similar properties (**Fig. 2c** and **Fig. S2**) and resulted in significantly better predictions in different training-validation scenarios (**Fig. 2d**).

The final recognition code consists of 36 random forests: 12 random forests for each of the N-terminal, C-terminal, or middle ZF contexts, with each random forest predicting the preference for binding to one of the four possible bases at one of the three DNA triplet positions (**Fig. S1**). We benchmarked the performance of our C-RC using different evaluation schemes. First, we used 50 randomly selected ZF-target pairs from ChIP-seq data, which were excluded from all stages of the random forest training, including feature selection. As shown in **Fig. 2e**, C-RC outperformed a previous B1H-based recognition code (B1H-RC)[1] in predicting the base preferences for 11 out of 12 base-position combinations. Next, we compared the accuracy of C-RC with two available approaches, the B1H-RC[1] and ZFModels[5], using protein-binding microarray (PBM) data from a set of non-animal C2H2-ZFPs[10] and a set of synthetic C2H2-ZFPs created from concatenating different ZFs from different proteins[22]. C-RC produced motifs that were significantly more similar to the PBM motifs than both B1H-RC and ZFModels predictions in both datasets (**Fig. 2f,g**), suggesting that the new code outperforms the state-of-the-art irrespective of the nature of the reference data (*in vivo* or *in vitro*) or the source of the protein (human, non-animal, or synthetic).

The new recognition code reflects known and novel structural features of ZF-DNA interaction

Random forests are ensembles of large number of trees, which are not directly interpretable. To understand how C-RC works, we examined the output of the code for 100,000 randomly generated ZFs, each with one adjacent ZF on each side. By correlating the output of C-RC with the amino acid identities at each of the central or adjacent ZF positions, we were able to obtain a simplified picture of the average effect of each amino acid at each position on the recognition of different bases. This simplified representation ignores more complicated features that might be encoded in the random forest model, such as the non-linear dependencies of different positions. Nonetheless, it reveals key features, such as the associations between different positions of the ZF and target the DNA. Many of these associations are consistent with the canonical model of ZF-DNA interaction as shown in **Fig. 3a**. However, the model also encodes strong associations that are not part of the canonical model, most prominently between position 3 of the DNA triplet and position +6 of the N-terminal neighboring ZF (**Fig. 3b**).

To understand whether these novel associations are structurally relevant, we performed MD simulations of the CCCTC-binding factor (CTCF) in complex with its cognate DNA, and indeed identified a non-canonical interaction between position +3 of the DNA triplet that is adjacent to ZF5 and residue +6 of ZF4 (**Fig. 3c,d**). Consistent with this observation, C-RC predicts that mutations in residue +6 of ZF4 on average negatively affect this interaction (**Fig. 3e**). In fact, systematic application of this *in silico* mutation strategy revealed a quantitative relationship between the associations predicted by C-RC and the strength of H-bonds observed in MD simulations, (**Fig. 3f**). This analysis suggests that C-RC not only enables the identification of non-canonical interactions, but also allows us to predict the strength of canonical interactions given the sequence of the ZFP and its target DNA.

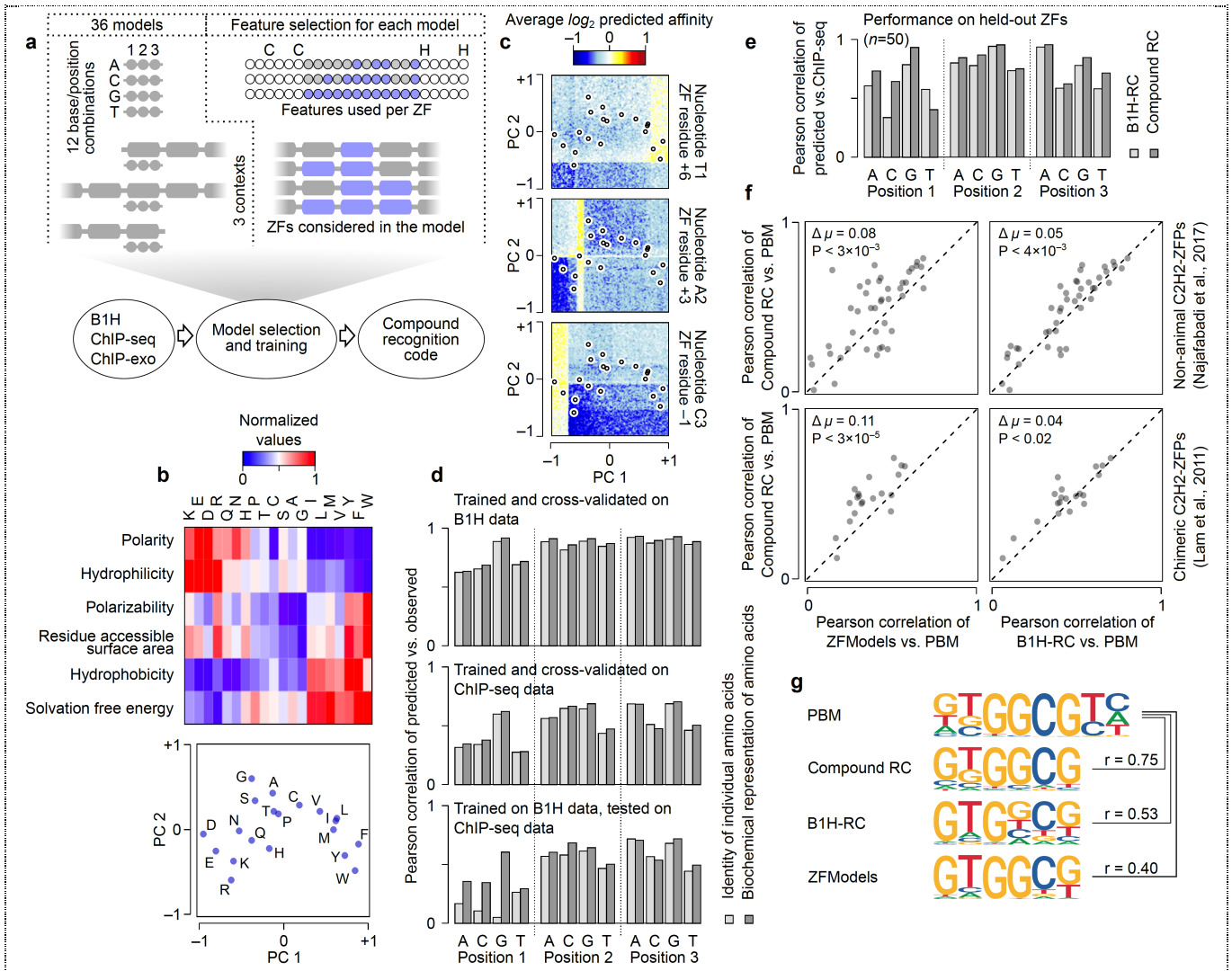

Figure 2. Training and evaluation of C-RC. (**a**) Schematic representation of the procedure for training C-RC. Thirty-six models were trained separately (top left), corresponding to recognition of four bases at three DNA positions in three different contexts. Feature selection for each model included selection of residues to be considered for each ZF, as well as the choice of ZFs (top right). See **Fig. S1** for detailed representation of the selected features for each model. (**b**) Encoding the amino acids by their biochemical properties. The heatmap (top) represents the biochemical properties we considered. The PCA-transformed values are shown in the scatterplot at the bottom. Underlying data are provided in **Table S3**. (**c**) Visual representation of example rules learned by random forest after encoding the amino acids by their biochemical properties. We generated 40,000 "pseudo-amino acids" by dividing the PCA plot in panel (b) into a 200×200 grid, and then generated 40,000 random ZFs by sampling (without replacement) these pseudo-amino-acids for each of the 12 ZF positions. The color gradient in the graphs shows the predicted affinity of these random ZFs for recognition of base T at position 1 of DNA triplet (T1), recognition of A2, or recognition of C3, as indicated beside each graph (see **Fig. S2** for additional base-position combinations). The ZFs are projected on the scatterplot based on the PCA coordinates of the pseudo-amino-acid at position +6, +3, or –1, as indicated beside each graph. (**d**) The performance of the recognition code for predicting the probability of each base at each triplet position, when the amino acids are encoded as categorical variables (20 individual identities) or using the PCA-transformed biochemical properties. We used 5-fold cross-validation on B1H motifs[1] (top) or ChIP-seq motifs[18] (middle), or trained the recognition code on B1H motifs and tested on ChIP-seq motifs (bottom), ensuring that any ZF present in the ChIP-seq data was removed from the B1H training set. (**e**) Comparison of the performance of C-RC and a B1H-based recognition code[1] (B1H-RC) for predicting the base probabilities at different triplet positions for 50 ChIP-seq ZFs that were excluded from the feature selection procedure and model training. (**f**) Systematic comparison of C-RC, B1H-RC, and ZFModels predictions vs. PBM motifs from non-animal C2H2-ZFPs[10] and chimeric C2H2-ZFP constructs[22]. Pearson correlation similarity of motif pairs are calculated by MoSBAT-e[23]. P-values are based on two-tailed paired t-test. (**g**) As an example, MoSBAT-e comparison of the motifs predicted by C-RC, B1H recognition code, and ZFModels[5] vs. the motif obtained by PBM[10] for a C2H2-ZFP from *Rhizopus delemar* (UniProt ID I1BM86) is shown.

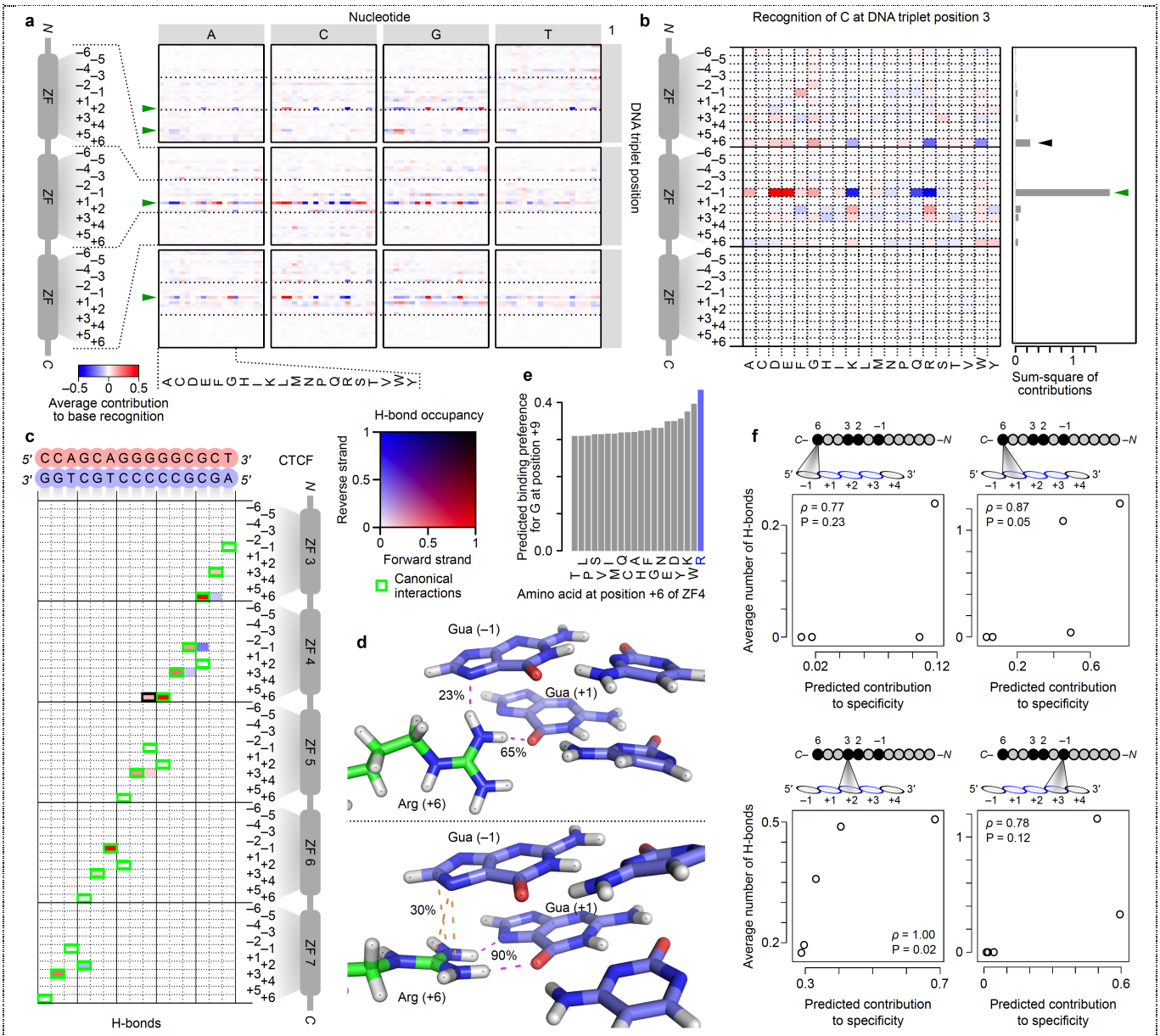

Figure 3. C-RC quantitatively predicts amino acid-base interactions. (**a**) The average contribution of each amino acid at different ZF positions for recognition of each base at different DNA triplet positions. Each panel represents recognition of one base, indicated above the figure, in a specific DNA triplet position, indicated on the right; each column represents one amino acid, each row represents one ZF position, and the color gradient denotes the contribution toward specificity (red: increased preference for the specified base; blue: decreased preference). The specificity residues that, according to the canonical model, contribute to the recognition of each DNA position are shown with green arrows. (**b**) Recognition of base C at position 1 of the DNA triplet. The bar graph on the right shows the squared sum of values at each ZF position. The black arrow represents a potential new interaction with position +6 of the N-terminal neighboring ZF. (**c**) H-bonds identified from MD simulations of CTCF in complex with its target DNA. The interactions in the canonical C2H2-ZF model are shown with green border. The non-canonical interaction highlighted in panel b is shown here with black border. Underlying data are provided in **Table S4**. (**d**) The Arginine at position +6 of ZNF4 forms a non-canonical interaction with position –1 of its cognate DNA triplet. The interaction exists in two dominant conformations: a hydrogen bond (23% of MD simulation frames) between the Arginine and the base (top) and a stacking overlap (30%) between Arginine and the guanidino group and the DNA base (bottom). (**e**) The predicted preference of variants at position +6 of ZF4 for binding to G at DNA position 9 (i.e. position –1 relative to the ZF4-associated triplet). The wild-type amino acid is highlighted in blue. (**f**) Scatterplots for the recognition code-predicted associations vs. MD simulation-based H-bonds. In each plot, each dot represents one ZF. The graphs represent the amino acid-base pairs for which at least one H-bond and at least one non-zero association based on the recognition code was found. The spearman correlations are shown, along with their associated P-values (two-tailed).

A domain-resolution map of *in vivo* DNA binding reveals broad conservation of DNA-binding ZFs and low conservation of non-binding ZFS

Human C2H2-ZFPs on average contain ~10 ZFs per protein[1], which is substantially longer than what would be expected from the binding preference of most transcription factors, suggesting that only a fraction of the ZFs of most proteins engage with DNA. Combining *in vivo* binding data with the predicted DNA preferences of the ZFs enables the identification of the ZF domains that engage with DNA *in vivo*[24]. We therefore sought to combine our new recognition code with the genomic binding sites of human C2H2-ZFPs to characterize their *in vivo* binding preferences and the ZF domains that engage with the DNA. We used a previously described framework[24], which starts by predicting the binding preferences of all possible ZF arrays contained in a C2H2-ZFP. It then identifies the ZF array whose binding preference maximally explains the observed *in vivo* binding sequences, along with its optimized binding motif. We applied this framework to previously published ChIP-seq and ChIP-exo data[18,19], limiting the results to cases where the C-RC predictions and *in vivo*-optimized motifs had significant similarity at $P<0.001$. We identified significant motifs for 109 ChIP-seq and 126 ChIP-exo datasets (**Fig. 4a** and **Fig. S3**, respectively), encompassing a total of 209 unique proteins.

Several lines of evidence from the analysis of the *in vivo* data point to substantially improved performance of the C-RC compared to the state-of-the-art, adding to the benchmarking results presented in the previous sections. First, in both ChIP-seq and ChIP-exo data, the C-RC was able to predict *in vivo*-enriched motifs for more C2H2-ZFPs than B1H-RC (**Fig. 4b**). Particularly, in the ChIP-exo data, the new recognition code was able to increase the number of proteins with significant motifs by ~25%. Secondly, for datasets that produced significant motifs using both the B1H-RC and the new recognition code, C-RC was able to identify a larger number of ZFs that engage with DNA (**Fig. 4b**). Thirdly, for these common proteins, the motifs identified by C-RC had overall higher quality, as measured by the area under the receiver operating characteristic curve (AUROC) for distinguishing real binding sites from dinucleotide-randomized sequences (**Fig. 4b**).

Based on the motifs identified by combining C-RC and ChIP-seq data, on average about 56% of the ZFs of each protein appear to engage with DNA *in vivo* (45% for ChIP-exo data), although these ZFs vary substantially in terms of their sequence specificity, as measured by the information content of the 3-nucleotide motif that corresponds to each ZF (**Fig. 4a** and **Fig. S3**). Interestingly, we observed that DNA-engaging ZFs are overall more conserved across vertebrates than non-binding ZFs or ZFs that bind to DNA with low sequence specificity (measured by information content of their associated motifs). This trend can be seen when we aggregate all ZFs from all C2H2-ZFPs that have ChIP-seq data (**Fig. 5a**), as well as when we analyze the ZF domains of each C2H2-ZFP individually (**Fig. 5b**). We also separately analyzed the conservation pattern of ZF domains in C2H2-ZFPs that contain a KRAB domain – these C2H2-ZFPs are relatively recent and are often involved in repression of transposable elements[1,9,18,19]. Surprisingly, despite their overall lower conservation across vertebrates, likely due to their more recent origin, the correlation between conservation and DNA-binding can be clearly seen in KRAB-containing C2H2-ZFPs (**Fig. S4a**), suggesting that DNA-binding ZFs are more conserved than non-binding ZFs both in KRAB-containing and non-KRAB C2H2-ZFPs.

The higher conservation of DNA-engaging ZFs suggests that mutations in these regions are overall more deleterious than mutations in ZFs that do not bind DNA (which may potentially have other functions). We set out to confirm this hypothesis by analysis of population-level genetic variations in human ZFs. Using genetic variation data from gnomAD, which encompasses variants identified from >140,000 individuals, we observed that missense variations in ZFs that engage with DNA with high specificity are significantly less frequent than missense variations in ZFs that do not engage with DNA or have low sequence specificity (**Fig. 5c**). We also specifically examined the frequency of rare missense variants (minor allele frequency $< 10^{-5}$) and more common variants (minor allele frequency > 0.001), reasoning that extremely rare variants are likely to be recent and, therefore, have not been filtered by negative selection yet, as opposed to common variants[25]. We noticed that common variants are significantly depleted from DNA-engaging ZFs compared to non-binding or low-specificity ZFs (**Fig. 5d**), suggesting that these ZFs are under stronger negative selection. This trend holds for both KRAB-containing C2H2-ZFPs and non-KRAB C2H2-ZFPs (**Fig. 5d**), confirming the pattern that we observed by analysis of ZF conservation across vertebrates. Nonetheless, we observed overall stronger depletion of common variants in non-KRAB C2H2-ZFPs, to the extent that non-DNA-binding ZFs of these proteins appear to harbor the same ratio of common and rare variants as DNA-binding ZFs of KRAB proteins (**Fig. 5d**). This trend suggests a stratified model of selective pressure on the ZFs based on their function, in which mutations at the DNA-binding ZFs of non-KRAB proteins are overall the most deleterious ones, whereas mutations at the non-DNA-binding ZFs of KRAB proteins are least affected by negative selection (**Fig. 5e**).

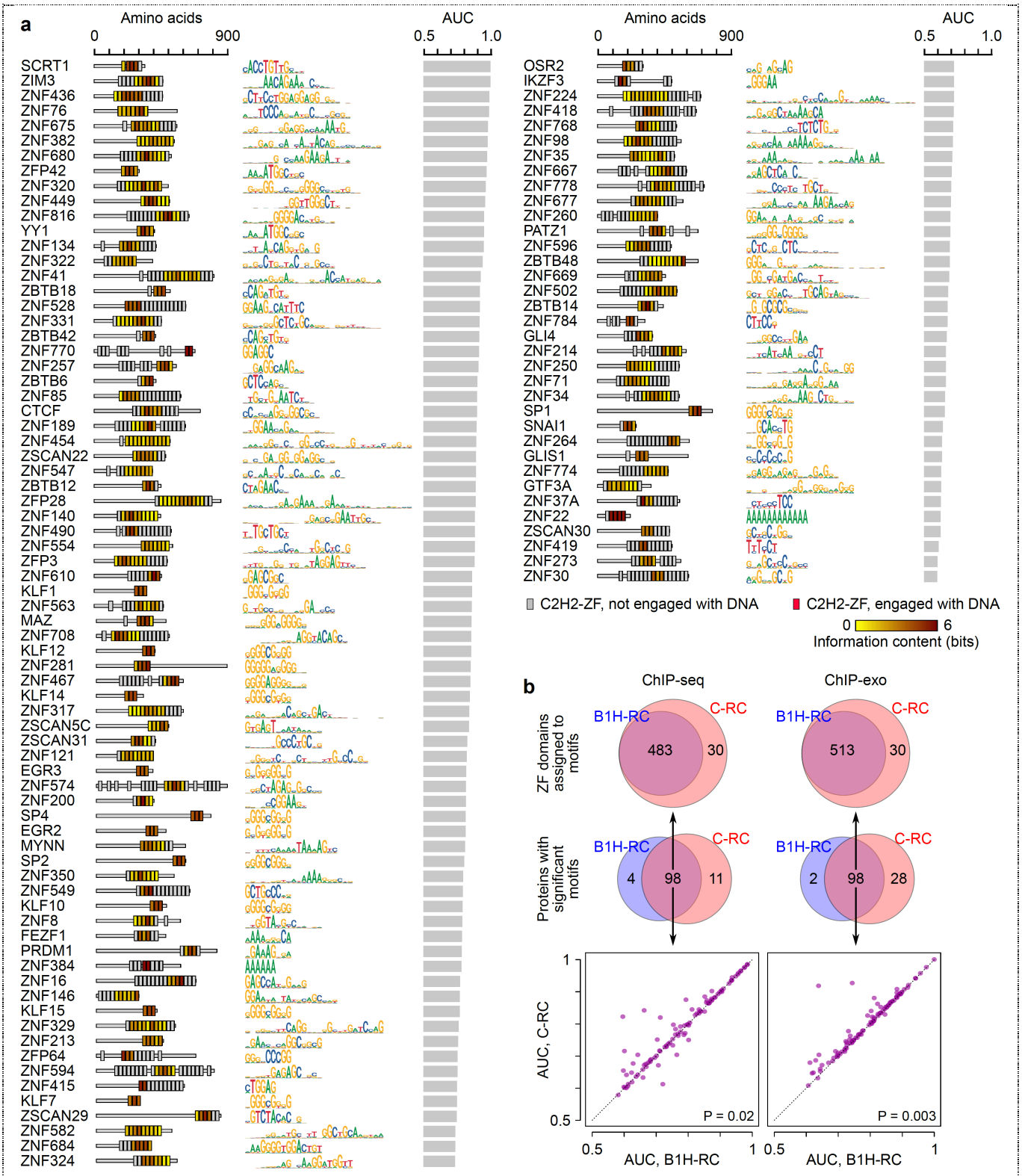

Figure 4. C-RC improves identification of motifs and the associated ZFs from *in vivo* data. (**a**) Motifs identified by recognition code-assisted analysis of ChIP-seq data for C2H2-ZFPs. For each protein, the domain structure is shown on the left (only the ZF domains). The bar graph shows the AUROC for distinguishing the binding site sequences from dinucleotide-shuffled sequences. The ZFs that correspond to the identified motifs are highlighted, with the colour gradient representing the sequence-specificity of the ZF (as measured by information content). See **Fig. S3** for ChIP-exo motifs. Position-specific frequency matrices are provided in **Data Files S1 and S2**. (**b**) Comparison of the number of motifs (middle) and the number of ZFs associated with the motifs (top), as identified by the B1H-RC or C-RC using ChIP-seq data[18] (left) or ChIP-exo data[19] (right). For common motifs, the AUROC values of the optimized versions are compared in the scatterplots at the bottom.

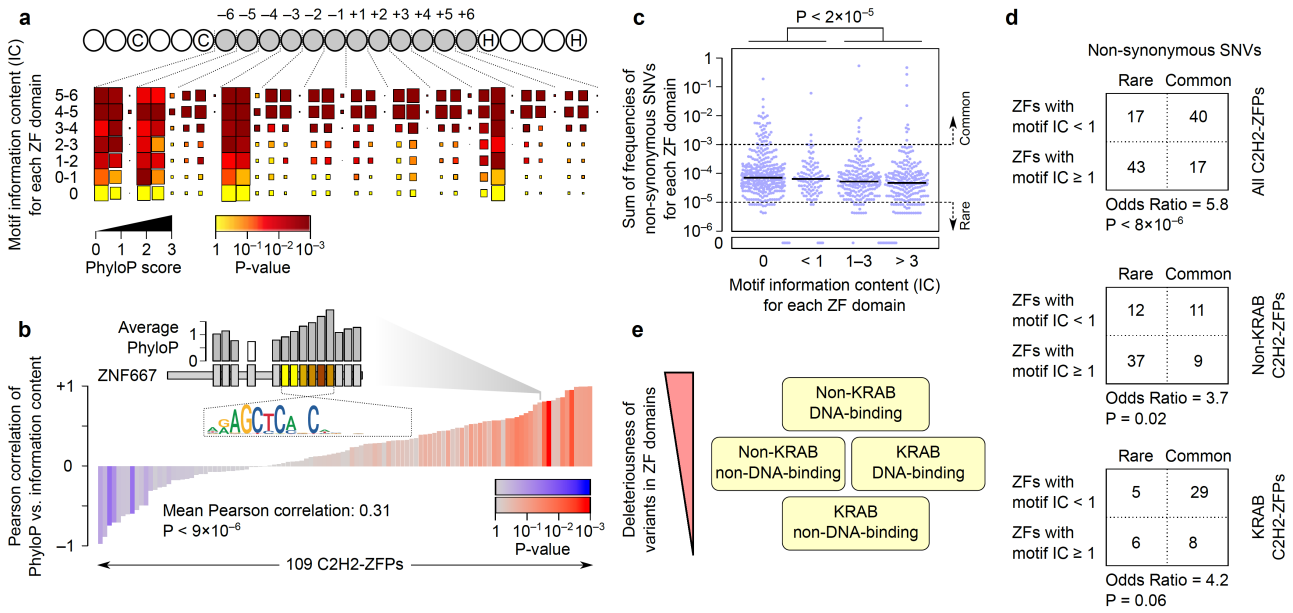

Figure 5. DNA-binding ZFs are under stronger purifying selection for both KRAB and non-KRAB C2H2-ZFPs. (**a**) PhyloP[26] conservation score profile across ZFs that do not engage with DNA (i.e. IC=0) and those that engage with varying sequence-specificity. Each set of three columns represents one codon in the ZF-encoding sequence, and each row represents one set of ZFs, binned by the information content (IC) of their associated triplet in the *in vivo* motif. The box size represents the average phyloP score, whereas the color gradient represents the difference of conservation compared to ZFs that do not engage with DNA (P-value based on one-tailed t-test). Data provided in **Table S5a**. (**b**) Correlation of the phyloP score profile of each C2H2-ZFP with the IC of the ZFs. The inset illustrates an example in which the phyloP score of the ZFs (bar plot above the ZNF667 domain structure) correlates with the IC of the ZF-associated triplets (color of the ZF domains, similar to **Fig. 4a**). For each C2H2-ZFP, the P-value associated with the Pearson correlation is shown using the color of the associated bar (two-tailed correlation t-test). The overall P-value for deviation of the mean of correlations from zero is also shown (two-tailed t-test). Also see **Fig. S4**. (**c**) Minor allele frequencies of non-synonymous variants for ZFs that do not engage with DNA (IC=0), ZFs with low sequence-specificity (IC<1), and ZFs with high sequence-specificity (IC≥1). Each dot represents one ZF, and the y-axis shows the sum of frequencies of all non-synonymous minor alleles that overlap with the ZF. P-value is based on two-tailed t-test. Data provided in **Table S5b**. (**d**) Overlap of rare and common non-synonymous variants with ZFs that engage with DNA with high specificity (IC≥1) and ZFs that do not engage or have low specificity (IC<1). The top table represents all C2H2-ZF proteins with ChIP-seq-based motifs, whereas the next two tables are stratified based on absence or presence of a KRAB domain in the protein. (**e**) A schematic model showing the inferred deleteriousness of variants in different ZFs, as suggested by the frequencies of common and rare variants.

Mutations in DNA-binding ZFs accompany widespread expression changes in target genes across cancers

The tight association between conservation and DNA-binding ability across all ZF residues (**Fig. 5a**) implies that mutations in the majority of ZF positions are detrimental to the ZF-DNA interaction. Given that C2H2 zinc fingers are frequently mutated in cancer[27], we studied transcriptome changes associated with ZF somatic mutations across 2538 tumour samples and 18 cancer types[28] (**Table S6**), in order to understand the gene regulatory consequences of these mutations. For each C2H2-ZFP, we selected the samples with no copy number alterations (CNAs) at the ZFP locus, and then modeled the association between expression of each gene and the presence of at least one missense mutation in the DNA-binding zinc fingers of the C2H2-ZFP, while correcting for the confounding effect of tissue of origin (cancer type), the cancer type-specific effects of sex and age, and CNAs at the target gene (see **Methods**). This pan-cancer meta-analysis revealed substantial association between genome-wide gene expression and somatic mutations at the DNA-binding ZFs of specific C2H2-ZFPs (**Fig. 6a**, **Data File S3**).

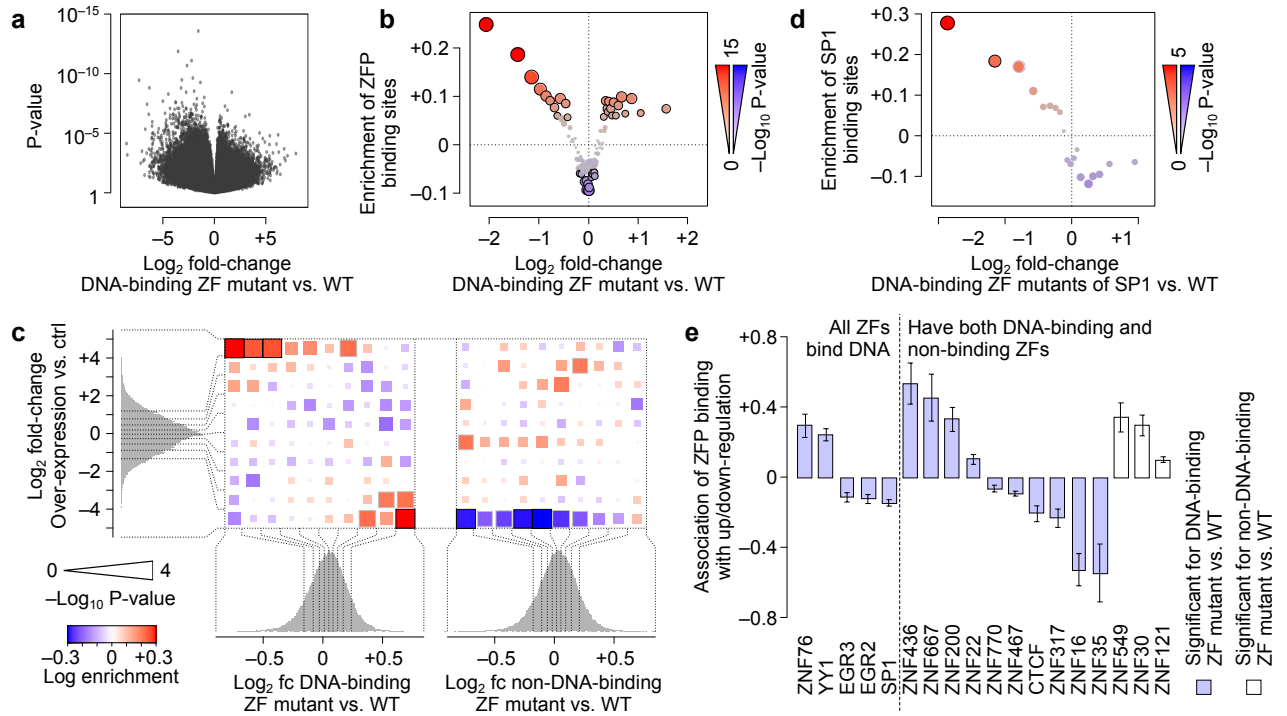

Figure 6. Expression of ZFP target genes are associated with somatic mutations in DNA-binding ZFs. (**a**) Volcano plot for association of gene expression and somatic mutations in DNA-binding ZFs for 1,304,830 gene-ZFP pairs. The x-axis represent the effect size of the somatic mutation, and the y-axis represents the associated P-value. (**b**) Enrichment of ChIP-seq-based ZFP-gene regulatory connections among the ZFP-gene pairs with varying degrees of mutation-expression association. ZFP-gene pairs were grouped into 100 equally populated bins based on the mutation effect size (x-axis) and, in each bin, the enrichment of ZFP-gene pairs that represent a ChIP-seq-based regulatory link relative to expectation was calculated (see **Methods**). The y-axis represents log-odds of regulatory links, each circle represents one bin, and the circle size/color represents P-value (logistic regression). (**c**) For 63 ZFPs that have RNA-seq data from over-expression in HEK293 cells[18], we binned the ZFP-gene pairs based on the joint distribution of the effect sizes of ZFP over-expression (y-axis) and somatic mutations (x-axis) in DNA-binding ZFs (left) or non-DNA-binding ZFs (right). For each bin, the log-odds for ChIP-seq-based ZFP-gene regulatory links relative to expectation is shown using the color of boxes in the heatmap, while the size of the boxes correspond to P-value (logistic regression, see **Methods**). The histograms and the dotted lines represent the distribution of effect sizes and the boundaries of the bins. (**d**) Similar to panel (b) but limited to SP1-gene pairs. Genes are binned into 20 equally populated bins based on the effect size of SP1 mutation. (**e**) C2H2-ZFPs whose ChIP-seq-based regulatory targets are enriched among genes that are positively or negatively associated with the ZFP somatic mutation. A logistic regression was used to assess the significance of the association between the presence of a peak near gene TSS and the effect size of mutation on gene expression (see **Methods**), separately for somatic mutations in DNA-binding ZFs (blue bars) and non-DNA-binding ZFs (white bars). The y-axis shows the regression coefficient, and the error bars represent standard error of mean. Only significant ZFPs (FDR<0.005) are shown.

Several lines of evidence suggest that these ZFP-gene associations reflect bona fide regulatory interactions: First, we observed a significant overlap between the ZFP-gene associations we identified by analysis of somatic mutations and the direct ZFP-gene associations identified by ChIP-seq (**Fig. 6b**). Secondly, this overlap is consistent with disruption of ZFP function, as revealed by analysis of RNA-seq data from over-expression of 63 ZFPs[18] (**Table S7**): we found that direct ZFP targets (based on ChIP-seq) overall respond in opposite directions to somatic mutations and ZFP over-expression (**Fig. 6c**). Specifically, *in vivo* ZFP binding site are enriched among genes that are up-regulated as a result of ZFP over-expression and down-regulated in samples with somatic mutations in DNA-binding ZFs. A similar pattern can be seen for genes that are down-regulated after ZFP over-expression and up-regulated in mutant samples. In contrast to somatic missense mutations in DNA-binding ZFs, somatic mutations in ZFs that do not bind DNA *in vivo* did not show such a pattern (**Fig. 6c**), suggesting that only mutations in DNA-binding ZFs have a transcriptomic signature that opposes phenotypic activation of the ZFP.

Thirdly, we found that the direct regulatory targets of each ZFP (**Data File S4**) overall show a consistent response to somatic mutations in DNA-binding ZFs. For example, SP1 binding sites are specifically enriched near the transcription start sites (TSS's) of genes that are down-regulated as a result of SP1 mutation (**Fig. 6d**). Overall, we found 15 ZFPs in which somatic mutation of DNA-binding ZFs leads to a consistent response in their

direct targets (FDR < 0.005). In contrast, somatic mutations of non-DNA-binding ZFs showed a similarly significant pattern in only three ZFPs (**Fig. 6e**). Finally, we observed that loss of heterozygosity (LOH) in each ZFP locus leaves a gene expression signature that is highly consistent with that of somatic missense mutations in DNA-binding ZFs (**Fig. 7a**), suggesting that somatic mutations of DNA-binding ZFs, which are often monoallelic, have regulatory effects similar to LOH.

Gene expression signatures of somatic mutations demarcate ZFP regulons

The above results enabled us to identify the set of genes whose expression is significantly affected by the missense mutations that disrupt DNA-binding capability of each C2H2-ZFP, which should represent part of that ZFP's regulon, including direct and/or indirect targets. To increase statistical power, we leveraged the LOH-associated gene expression changes, and used them as a prior to identify mutation-associated expression changes using independent hypothesis weighting (IHW[29]) (**Fig. 7b**). Overall, we identified 3366 significant ZFP-gene associations (FDR < 0.2) between 2456 genes and 95 C2H2-ZFPs (**Fig. 7c**, **Table S8**). The size of the identified ZFP regulons ranged from only 1 gene for ZNF35 to 201 genes for ZBTB48, suggesting varying degrees of power for detecting gene regulatory effects of different ZFPs based on analysis of somatic mutations.

To evaluate the fidelity of these regulons, we examined the agreement between our mutation-based ZFP-gene associations and the co-expression of ZFP-gene pairs. Genes that are part of a TF's regulon (including direct and indirect targets of the TF) often show coordinated expression across different samples in way that reflects the expression level of the TF itself. Therefore, we expect the genes that are dysregulated as a result of a ZFP mutation to be associated with that ZFP's expression if they are part of the ZFP regulon. This association should be observed even across samples that have neither CNA nor any mutation at the ZFP locus (an example is shown in **Fig. 7d**). Overall, we observed a trend consistent with this expectation across multiple cancer types: We identified 83 ZFP-cancer pairs for which there was a significant association between mutation-based regulatory links and co-expression. Among these significant associations, ~81% (67 out of 83, binomial $P<10^{-8}$) had the expected direction, i.e. genes that were down-regulated as a result of ZFP mutation were positively correlated with ZFP expression, and mutation-up-regulated genes were negatively correlated with ZFP expression (**Fig. 7e**). Together, these results support the notion that somatic missense mutations in DNA-binding ZFs hamper the regulatory function of the ZFPs, allowing identification of their direct and indirect targets.

Discussion

Our analyses indicate that the compound recognition code (C-RC) provides a more accurate model of DNA binding by C2H2-ZFs than existing models, as a result of incorporating *in vivo* binding data during model construction. Interestingly, this improvement was achieved by inclusion of *in vivo* binding preferences of less than 840 human zinc fingers, leaving open the possibility of further improvements as additional *in vivo* data become available for C2H2-ZFPs. Furthermore, our molecular dynamics analyses suggest that C-RC can quantitatively infer the contribution of different ZF residues to DNA specificity, including new potential interactions beyond the canonical model such as π-π stacking of planar amino acids with DNA bases. These interactions appear to occur as a result of alternate conformations of the amino acid side chains at the DNA-protein interface – this might explain why they were not reported earlier in the X-ray crystal structures of C2H2-ZPFs, which often represent only the most stable conformation.

By combining the C-RC with ChIP-seq and ChIP-exo data, we were able to obtain a domain-resolution map of ZFP-DNA interactions for a total of 209 C2H2-ZFPs, which suggested that ~50% of ZF domains engage with DNA *in vivo*. We observed that DNA-engaging ZFs are more conserved across species than ZF domains that do not engage with DNA. This trend in conservation, however, is not limited to the base-contacting residues and can be observed in all ZF residues, suggesting that non-base-contacting residues are also under stronger selective pressure in ZFs that engage with DNA compared to ZFs that do not engage with DNA *in vivo*. This observation is consistent with a role of non-base-contact residues in DNA-binding (e.g. through interaction with DNA backbone, as suggested by recent studies[10]). On the other hand, the relative lower sequence conservation in ZFs that do not bind DNA may reflect alternative functions that allow higher tolerance to mutations in the protein sequence.

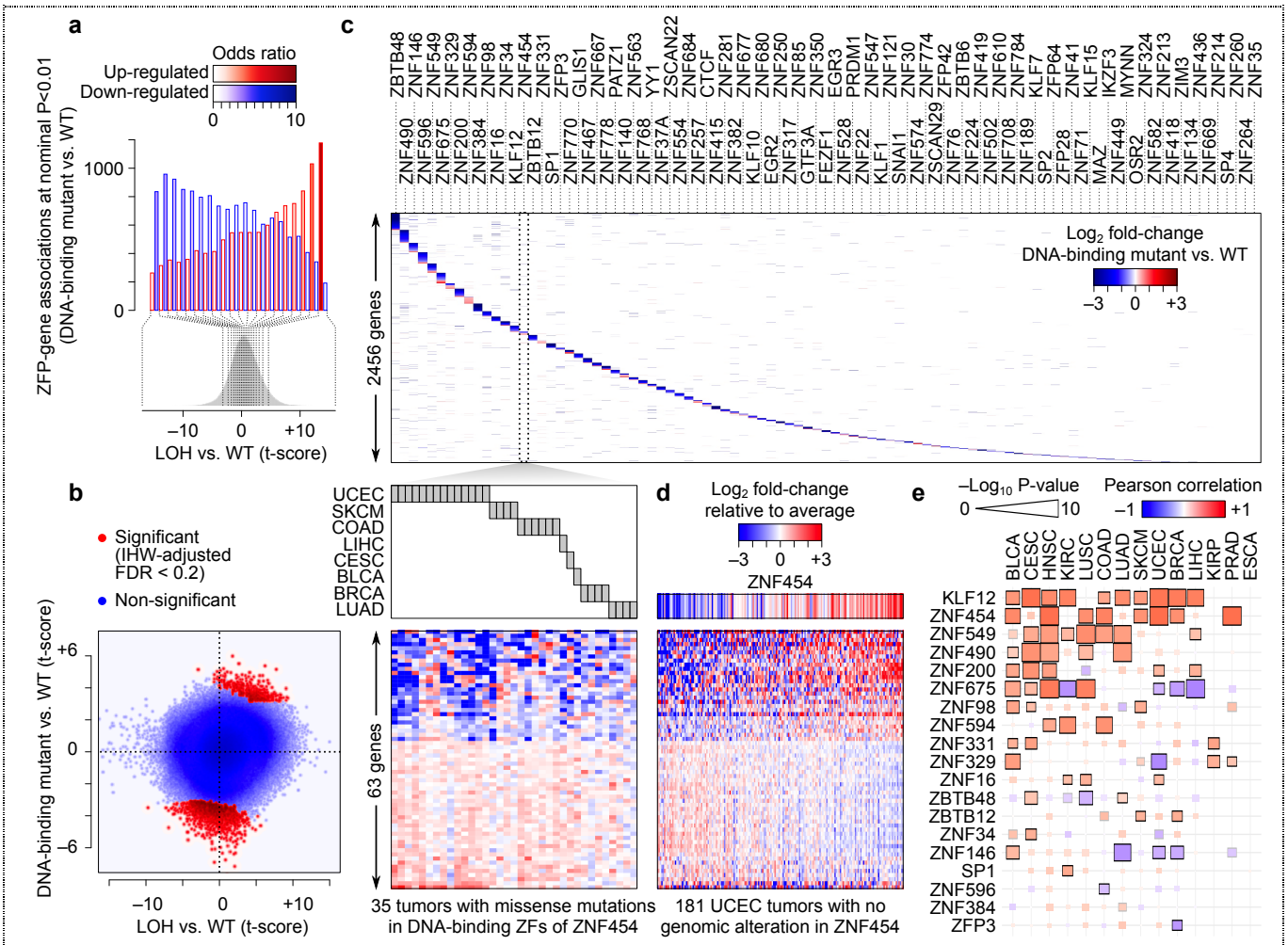

Figure 7. Gene expression signatures of somatic mutation in DNA-binding ZFs. (**a**) Consistence between the effect of ZFP somatic mutations and ZFP loss-of-heterogeneity (LOH). ZFP-gene pairs were grouped into 20 bins based on the expression effect size of ZFP LOH (x-axis), and within each sample, the number of ZFP-gene pairs that pass P-value threshold of 0.01 for positive association or negative association with somatic mutation was calculated (y-axis). The color gradient shows the log-odds of positive mutation effect size (red) or negative mutation effect size (blue). (**b**) Identification of significant associations between ZFP somatic mutation and gene expression, using the association between ZFP LOH and gene expression as a prior for increased statistical power. Each dot represents one ZFP-gene pair, with significant gene pairs (IHW-adjusted FDR<0.2) shown in red. (**c**) Heatmap of significant ZFP-gene associations (top). Each column is one ZFP, each row is one gene, and the colour gradient shows the size of the effect of somatic mutation in the DNA-binding ZFs of each ZFP on the expression of each gene. As an example, genes that are significantly associated with DNA-binding ZF mutations in ZNF454 are shown at the bottom heatmap, with each column representing one mutation-containing tumour sample. The cancer type of each sample is shown on top of the heatmap. (**d**) The correlation between ZNF454 expression across UCEC tumours and expression of its regulon. Each row is a gene, in the same order as the bottom heatmap of panel (c). Each column is one sample, limited to those that do not have any somatic alteration in the ZNF454 locus. (**e**) Concordance between ZFP mutation effect size and ZFP-gene co-expression. For each ZFP and each cancer type, the Pearson correlation between the genome-wide effect size of somatic DNA-binding ZF mutation and the ZFP-gene expression correlations were calculated (see **Methods**). The color gradient shows the Pearson correlation, with red depicting correlations that are in the expected direction and blue representing correlations that are opposite of the expected direction. The box size shows the associated P-value (t-test). Significant Pearson correlations are shown with a black border (FDR<0.01) or grey border (FDR<0.05).

Interestingly, this pattern can be found not only in non-KRAB C2H2-ZFPs, but also in KRAB proteins, whose functions in regulating gene expression are less understood. This observation suggests that mutations in the DNA-binding domains of KRAB proteins are deleterious, which is also supported by depletion of common genetic variants in DNA-binding ZFs at the population level. This is a surprising finding given that there are few known disease-linked KRAB proteins, and highlights the need for better characterization of the functions of these proteins in genome regulation. In fact, our pan-cancer analysis revealed a substantial number of genes whose expression is significantly associated with somatic mutations in the DNA-binding ZFs of KRAB proteins (**Fig. 7b**), suggesting that mutations in these proteins have widespread consequences on the transcriptome.

A question that needs to be addressed is whether the KRAB proteins that we analyzed are representative of all KRAB-containing C2H2-ZFPs: We limited our analyses to the C2H2-ZFP binding sites that do not overlap with endogenous repeat elements (EREs) due to their confounding effect on motif finding[24]; however, a large

number of the KRAB protein binding sites are in EREs[1,18,19], which may result in the identification of high-quality motifs for fewer KRAB C2H2-ZFPs. Indeed, we were able to obtain high-quality motifs for only 25% of the KRAB proteins that almost exclusively bind to ERE regions (i.e. >90% of top 500 peaks in EREs). In contrast, for the rest of KRAB proteins, we had >97% success rate in finding high-quality motifs that match the recognition code predictions, suggesting that our results may be biased against exclusive ERE binders. We note, however, that this group likely forms a relative minority of KRAB proteins (12 out of 55 KRAB proteins with ChIP-seq data match our definition of exclusive ERE binder).

Our study of the *in vivo* DNA-binding ability of ZFs mirrors previous studies that have shown that, at least *in vitro* and when fused to ZF1-2 of the Egr1 protein, not all ZF domains are able to bind to DNA[1]. These studies suggest that there are intrinsic differences between DNA-binding and non-binding ZFs. Do these intrinsic differences explain the observation that only a fraction of human ZF domains engage with DNA *in vivo*? We have found that ZFs that bind to DNA *in vivo* have, on average, higher sequence specificity than ZFs that do not engage with DNA (**Fig. S4c**), as predicted by our recognition code. However, sequence specificity alone is a modest predictor of *in vivo* DNA binding. Furthermore, ZFs that do not engage with DNA *in vivo* have, on average, significantly higher sequence specificity than ZFs in pseudogenes (which are presumably non-functional), suggesting that at least some of the non-engaging ZFs are intrinsically capable of binding to DNA (**Fig. S4c**). This notion is also supported by direct comparison of our *in vivo* binding map with *in vitro* bacterial one-hybrid data[1], which shows that while there is a statistically significant overlap between ZFs that bind to DNA *in vitro* and *in vivo* (odds ratio=1.7, $P < 0.003$, Fisher's exact test), at least 15% of ZFs that do not engage with DNA *in vivo* are still capable of binding to DNA *in vitro* (**Fig. S4d**). This raises the possibility that DNA-binding capability is, at least to some extent, determined by the context, which may include the ZF position in the array as well as the identity of adjacent ZFs. More strikingly, ~55% of ZFs that do not bind DNA *in vitro* interact with DNA *in vivo*, often with high specificity, enforcing the notion that *in vitro* binding assays at best only partially reflect the *in vivo* function of ZFs.

Finally, we note the possibility that some ZFs may engage with DNA in alternative binding modes that we have not yet characterized. A few C2H2-ZFPs are known to employ alternative sets of ZFs to bind to DNA[15-17]. This observation suggests that some ZFs might be engaged only in a subset of *in vivo* binding sites – such ZFs would not be part of the core motifs that we have presented in this paper, which can potentially explain their higher-than-random sequence specificity. Therefore, the factors that determine the ability of ZFs to engage with DNA may depend not only on the C2H2-ZFP itself, but also on its binding sites.

Methods

Obtaining the data set of C2H2-ZF preferences for training the recognition code

We obtained the *in vivo* binding sites of 313 proteins from two previous studies[18,19], representing 131 proteins with ChIP-seq and 221 proteins with ChIP-exo data in HEK293 cells. The binding sites of each protein were directly downloaded from GEO datasets associated with these publications (GEO accessions GSE76494 and GSE78099). For each datasets, we ran RCADE[24] on the top 500 peaks that did not overlap any endogenous repeat elements (EREs), as described previously[30] (ERE coordinates were obtained from the RepeatMaser track of the UCSC Genome Browser[31]). For successful runs, we included the top-ranking motif of each protein in our training dataset. For the proteins that had both ChIP-seq and ChIP-exo data and resulted in a significant motif in both cases, we used the ChIP-exo motif, given the higher resolution of ChIP-exo compared to ChIP-seq. We split each motif into its constituent triplets (total of 836 triplets), and also extracted the ZF associated with each triplet, as well as the two ZFs on the two ends of each direct ZF. For the triplet at the 5' end of each motif, no ZF from the C-terminus of the associated ZF was used. Similarly, for the triplet at the 3' end of each motif, no ZF from the N-terminus of the associated ZF was used (see **Fig. S1** for a schematic representation). We set aside 50 randomly selected ZFs from this training dataset, so that they could be used at the end for testing the obtained model. We augmented the training dataset with *in vitro* B1H-based motifs from 8138 ZFs[1]. Since in these B1H experiments only the binding preference of a single ZF was queried at a time, the associated ZF of each motif does not have any N-terminal or C-terminal adjacent ZFs.

Biochemical encoding of amino acids

For each amino acid, we extracted six different biochemical properties[32] (**Table S3a**). Given the strong correlations among these properties, we used principal component analysis (PCA) and used the transformed coordinates of the amino acids on the first two components (**Table S3b**) for downstream analyses.

Feature selection and training of the recognition code

We considered four possible input configurations for predicting the preference of the ZF for a DNA triplet: (a) only the ZF that is directly in contact with the triplet, (b) the direct ZF plus its N-terminal neighbor, (c) the direct ZF plus its C-terminal neighbor, and (d) the direct ZF plus its two neighbors.

For each of these configurations, we considered different set of input features (**Figure S1b**): (i) only the four canonical residues of the ZFs (i.e. residues –1, +2, +3, and +6), (ii) the seven residues that showed the highest correlations with the DNA preference according to Chi-square test of *in vivo* data (i.e. residues –4, –2, –1, +1, +2, +3, and +6), and (iii) all 12 residues between the second Cys and the first His in the ZF (i.e. the X_{12} in the Pfam pattern $X_2CX_{2,4}CX_{12}HX_{3,4,5}H$). For each configuration a-d, we tried each feature set i-iii for predicting each of the four bases at each position of the triplet, and chose the feature set that maximized the Pearson correlation of predicted vs. target values during 5-fold cross-validation.

Finally, for each of the three possible ZF contexts, we compared the performances of the compatible configurations and selected the best-performing configuration by 5-fold cross-validation. The ZF contexts were: (1) ZFs that are at the N-terminus of the DNA-binding ZF array (compatible with configurations a and c), (2) ZFs that are at the C-terminus of the DNA-binding array (compatible with configurations a and b), and (3) ZFs that in the middle of the DNA-binding array (compatible with configurations a, b, c, and d). The configuration that was selected for each context and the corresponding feature set are shown in **Fig. S1c**.

Evaluating the performance of the final mode

After configuration- and feature-selection based on 5-fold cross-validation results, the final recognition code was tested on 50 randomly selected held-out ZFs that were not included at any stage of training. We used the Pearson correlation of predicted vs. observed base probabilities as the measure of performance. Also, we used MoSBAT-e[23] to compare the predictions of the code with motifs obtained from protein binding microarray analysis of a set of non-animal C2H2-ZFPs[10] or chimeric C2H2-ZFPs constructed from fusion of different ZFs[22].

Molecular dynamics simulations of Egr1 and CTCF

CTCF-DNA complex was obtained by combining two crystal structures (PDB accessions 5T0U, 5UND)[33], and EGR1-DNA complex was obtained from PDB accession 4X9J[34]. The simulations were carried out using AMBER16 package[35] with the *ff14SB* force field. The system was immersed in a rectangular box of TIP3P water

model[36] with neutralizing concentration of ions. Additionally, Na+/Cl–ions matching the ionic strength of 0.1 M were included. Each system was energy-minimized using 2500 steps of steepest descent followed by 2500 steps of conjugated gradient using a harmonic restriction on the solute with a value of 40 kcal/mol·Å. The heating process was carried from 0 to 300 K using Langevin dynamics and subsequently followed by equilibration for 500 ps (NPT). Finally, we carried out unrestrained MD for 1 μs under NPT conditions. The particle mesh Ewald (PME) method[37,38] was used to handle long-range electrostatic interactions and a cutoff of 12.0 Å was used for the simulations. SHAKE algorithm[39] was used to contain hydrogen bonds and to allow a longer integration step. All simulations were carried out with a time step of 2 fs using the *pmemd* module in AMBER16[40]. The *cpptraj* module was used for trajectory analyses[41]. The criterion for hydrogen bonding was set at ≤3.0 Å distance between electron donor atom and hydrogen of electron acceptor atom with 120-degree angle cutoff. Heavy atoms involved in stacking interaction were identified as described in MolBridge[42]. A perpendicular distance cutoff of 3.2 Å between the planar atoms was used. The simulated structure and contacts were visualized using PyMOL[43].

Identification of the *in vivo* binding preferences and DNA-engaging domains of human C2H2-ZFPs

We created a modified version of RCADE[24], called RCADE2, which uses our new compound recognition code (C-RC) to predict the binding preferences of different ZF arrays, evaluate their enrichment in *in vivo* binding sequences (compared to dinucleotide-shuffled sequences), and then optimize the motifs to maximize AUROC. RCADE2 is available at https://github.com/csglab/RCADE2, and includes features such as HTML output and integrated positional analysis of the identified motifs. Using RCADE2, we analyzed ChIP-seq and ChIP-exo data from two previous publications[18,19] as described above, including removal of peaks that overlapped EREs to ensure that our analyses are not confounded by sequence homology among repeat elements, and then using the summit position of the top 500 peaks with the largest scores (i.e. smallest p-values) for motif finding. For successful runs, we extracted the top-scoring optimized motif that had significant similarity with the seed motif (i.e. the motif predicted by C-RC) at $P < 0.001$, and marked the ZFs associated with that motif as the DNA-engaging ZFs. For each DNA-engaging ZF, we also calculated the information content of the 3-nucleotide motif that it encodes as $IC = \sum_{i,j} p_{i,j} log_2(4 \times p_{i,j})$, where $p_{i,j}$ denotes the probability of observing base j at position i of the triplet motif ($1 \leq i \leq 3$).

Analysis of cross-species conservation and population-level genetic variation at ZFs

We obtained missense single-nucleotide variants (SNVs) and their frequencies from the Genome Aggregation Database (gnomAD[44]) for genomic build GRCh37.24. Only single nucleotide variants that passed the high-quality filter in gnomAD (PASS filter) were included for further analysis. Multiple variants for the same genomic location were split using BCFTools. ZF domains were annotated based on the presence of Pfam pattern $X_2CX_{2,4}CX_{12}HX_{3,4,5}H$ in the protein sequence, and the SNVs from the canonical transcript were mapped to their corresponding amino acid residue in the ZF. To obtain per-residue genetic variation, allele frequencies of the three codon positions were summed. We used a similar approach to analyze per-base conservation at the ZF coding sequences, using phyloP[26] conservation scores that were obtained from the UCSC Genome Browser (phyloP46way track, hg19).

Identification of ZFP-gene associations based on ChIP-seq data

To identify genes that have a binding site for each ZFP near their TSS regions, we first identified the high-confidence set of peaks for each ZFP by simultaneous optimization of the peak-calling score cutoff and the motif hit score cutoff, similar to a previous approach[18]. Briefly, for each C2H2-ZFP, we first identified the affinity-based motif-match score of each peak using AffiMx[23]. We then identified a motif score cutoff to dichotomize the peaks, in a way that maximizes the Mann-Whitney U z-statistic of the difference of peak scores between the two peak sets. Similarly, we identified a peak score threshold that maximizes the Mann-Whitney U z-statistic of the difference of motif scores between peaks that pass that threshold and peaks that do not. Any peak that passed the optimized peak-score threshold was deemed a significant binding site, and any significant binding site that also passed the optimized motif-score threshold was deemed to have a match to the motif. Then, we associated a gene to a significant binding site if that binding site was within 10kb of the TSS of the gene (**Data File S4**).

Data for mutation/expression analysis across cancers

Somatic mutations, copy number alterations (CNA), patient metadata (including age and sex), and gene expression data of TCGA Pan-Cancer Atlas[28] were downloaded from cBioPortal[45]. Gene expression values were

normalized by division to the 75th percentile of the non-zero values of each sample. We retained only tumour samples that had all of the four data types mentioned above. We further filtered the samples to keep only those that had at least one missense mutation in at least one of the C2H2-ZFPs with ChIP-seq data that we studied here. We also removed datasets (tissues) for which there were fewer than 30 samples with at least one mutated C2H2-ZFP. These filters resulted in a total of 2538 tumour samples from 18 cancer types (**Table S6**). Missense mutations were then classified into those that overlap a DNA-binding ZF (i.e. ZFs that recognize, *in vivo*, a 3-nucleotide motif with IC ≥ 1; see previous sections), those that overlap a non-DNA-binding ZF, and those that do not overlap a ZF. A total of 96 C2H2-ZFPs had at least one mutation overlapping a DNA-binding ZF (**Table S6**), which were further analyzed for association of their mutations with genome-wide expression.

Identification of genes whose expression is associated with ZFP mutations

Gene expression data were first filtered to include only genes that had an expression value >0.01 in at least 25% of all samples. For each C2H2-ZFP *z*, we then selected the samples that did not have a CNA at the ZFP locus (i.e. CNA=0 based on the obtained data), and further normalized and log-transformed the expression values using voom[46]. Then, for each gene *i*, we fit a linear model to the normalized and log-transformed expression data across samples *j* in the form of $E_i \sim T+T\times S+T\times A+N_i+M_z$, where E_i is the vector of expression of gene *i* across samples, *T* is the vector of tissue of origin of the samples, *S* denotes the sex of the patients from which the samples were obtained, *A* represents the age of the patients, N_i denotes the CNA status of gene *i* across samples (with integer values ranging from –2 to +2), and M_z is the vector of mutation status of the C2H2-ZFP *z* across samples (non-mutated, mutation in a non-ZF region, mutation in a DNA-binding ZF, and mutation in a non-DNA-binding ZF). The coefficients of the variable M_z for DNA-binding ZF mutations, along with the associated P-values, were then used to identify genes whose expression is associated with DNA-binding-disrupting mutations. Overall, this approach is overall similar to a previous work on identification of *cis*-eQTLs based on somatic mutations[47], with the difference that we looked at *trans*-acting coding mutations, we aggregated the mutations by the function of the affected protein domain, and we did not include any hidden factors in the regression model – inclusion of hidden factors are necessary to correct for the global structure and correlations in gene expression data in order to identify *cis*-acting effects; however, gene-gene correlations are likely driven by *trans*-acting factors, and therefore we decided not to remove them.

Overlap of ChIP-seq-based regulatory links and expression-mutation associations

To examine whether expression-mutation associations represent regulatory relationships between ZFPs and genes, we calculated enrichment of ChIP-seq-based ZFP-gene regulatory links, as determined by presence of a ChIP-seq binding site within 10kb of TSS (see above). For **Fig. 6b-d**, we examined the enrichment of these regulatory links in ZFP-gene pairs that fall within a specific bin (binned by the effect size of DNA-binding ZF somatic mutations in **Fig. 6b** and **d**, and by the joint distribution of the effect size of LOH and somatic mutations in **Fig. 6c**). For each bin, we then performed a logistic regression in order to model the log-odds of presence of a regulatory link as a function of the bin in the form of $L \sim B$, where *L* is the log-odds that a ZFP-gene pair corresponds to a ChIP-seq-based regulatory link, and *B* is a binary vector indicating whether that ZFP-gene pair belongs to the bin that is being examined. We note that some genes have overall higher probability of being associated with at least one ZFP in our ChIP-seq compendium, which may represent a bias towards genes that are expressed in HEK293 cells[18]. To correct for this bias, in the logistic regression, we considered the presence of a regulatory link between the ZFP and the gene as a "success", and the number of ChIP-seq-based regulatory links that connect that gene to "other" ZFPs as the number of "failures". Therefore, for example, if gene *x* has at least a peak for ZFP *z*, and also at least one peak for *n* other ZFPs, then the regression assumes $n+1$ Bernoulli observations for the *x*-*z* pairs, in which 1 was a success and *n* were failure. On the other hand, if gene *x* didn't have a peak for ZFP *z*, then there would be 0 success and *n* failures. We used a similar logistic regression for **Fig. 6e**, with the difference that the predictor variable, instead of being a binary vector, was the ZFP mutation effect size.

Identification of genes whose expression is associated with loss-of-heterozygosity (LOH) of ZFPs

We performed another association analysis, similar to the regression approach mentioned above, to identify genes whose expression is affected by LOH of each C2H2-ZFP. Specifically, for each C2H2-ZFP *z*, we excluded all samples that had any mutations in the ZFP coding sequence as well as samples that had biallelic deletion or copy number gains at the ZFP locus, normalized and log-transformed the resulting expression matrix using voom[46], and then fit a model of the form $E_i \sim T+T\times S+T\times A+N_i+N_z$, where N_z is the binary vector of CNAs for C2H2-ZFP *z* across the samples (0 for no CNA, 1 for LOH).

Identification of significant associations between gene expression and somatic mutations

We observed that LOH-associated gene expression changes are highly consistent with gene expression changes that are associated with mutations in DNA-binding ZFs. Therefore, we used LOH association to form a prior for P-value adjustment and detection of significant mutation associations. Specifically, we used independent hypothesis weighting (IHW[29]) to give a weight to each ZFP-gene pair based on the t-score of the coefficient of N_z in the LOH-expression association analysis, and then use these weights to maximize statistical power for detection of significant mutation-expression associations at FDR < 0.2.

Concordance between gene signatures of each ZFP and ZFP-gene co-expression

For each ZFP *z* and each cancer type, we modeled the expression of each gene *i* as a linear function of the expression of the ZFP across samples, taking into account the confounding effects of age and sex and the CNAs at the query gene locus: $E_i \sim S+A+N_i+E_z$, where E_z is the vector of expression of ZFP *z* across tumours. Then, for each ZFP, we calculated the Pearson correlation between the coefficients of E_z across the genes that are part of the ZFP regulon (based on association with ZFP mutation, see above) and the ZFP mutation effect size. Note that since the effect of somatic mutations in DNA-binding ZFs is expected to be negative for co-expressed ZFP-gene pairs and positive for anti-correlated ZFP-gene pairs, the Pearson correlation sign is inverted.

Acknowledgements

This work was supported by funds from the Natural Sciences and Engineering Research Council of Canada (RGPIN-2018-05962 to H.S.N) and resource allocations from Compute Canada. H.S.N holds a Canada Research Chair funded by the Canadian Institutes of Health Research. B.D. is supported by a postdoctoral fellowship from the Scientific and Technological Research Council of Turkey (TUBITAK, grant no. 1059B191600423). A.H.C. is supported by a Globalink Graduate Fellowship from Mitacs.

Author contributions

B.D. and H.S.N. developed the computational methods and analyzed the data. S.K. performed the structural analyses and contributed to analysis of genetic variations. A.H.C. contributed to data analysis and algorithm implementation. N.K. contributed to collection and processing of cancer data. H.S.N. conceived and directed the study. H.S.N wrote the manuscript with contribution from B.D. and S.K.

References

1. Najafabadi, H.S. *et al.* C2H2 zinc finger proteins greatly expand the human regulatory lexicon. *Nat Biotechnol* **33**, 555-62 (2015).
2. Wolfe, S.A., Nekludova, L. & Pabo, C.O. DNA recognition by Cys2His2 zinc finger proteins. *Annu Rev Biophys Biomol Struct* **29**, 183-212 (2000).
3. Pavletich, N.P. & Pabo, C.O. Zinc finger-DNA recognition: crystal structure of a Zif268-DNA complex at 2.1 A. *Science* **252**, 809-17 (1991).
4. Nardelli, J., Gibson, T.J., Vesque, C. & Charnay, P. Base sequence discrimination by zinc-finger DNA-binding domains. *Nature* **349**, 175-8 (1991).
5. Gupta, A. *et al.* An improved predictive recognition model for Cys(2)-His(2) zinc finger proteins. *Nucleic Acids Res* **42**, 4800-12 (2014).
6. Persikov, A.V. *et al.* A systematic survey of the Cys2His2 zinc finger DNA-binding landscape. *Nucleic Acids Res* **43**, 1965-84 (2015).
7. Persikov, A.V., Osada, R. & Singh, M. Predicting DNA recognition by Cys2His2 zinc finger proteins. *Bioinformatics* **25**, 22-9 (2009).
8. Myers, S. *et al.* Drive against hotspot motifs in primates implicates the PRDM9 gene in meiotic recombination. *Science* **327**, 876-9 (2010).
9. Jacobs, F.M. *et al.* An evolutionary arms race between KRAB zinc-finger genes ZNF91/93 and SVA/L1 retrotransposons. *Nature* **516**, 242-5 (2014).
10. Najafabadi, H.S. *et al.* Non-base-contacting residues enable kaleidoscopic evolution of metazoan C2H2 zinc finger DNA binding. *Genome Biol* **18**, 167 (2017).
11. Garton, M. *et al.* A structural approach reveals how neighbouring C2H2 zinc fingers influence DNA binding specificity. *Nucleic Acids Res* **43**, 9147-57 (2015).
12. Barazandeh, M., Lambert, S.A., Albu, M. & Hughes, T.R. Comparison of ChIP-Seq Data and a Reference Motif Set for Human KRAB C2H2 Zinc Finger Proteins. *G3 (Bethesda)* **8**, 219-229 (2018).
13. Brayer, K.J. & Segal, D.J. Keep your fingers off my DNA: protein-protein interactions mediated by C2H2 zinc finger domains. *Cell Biochem Biophys* **50**, 111-31 (2008).
14. Brown, R.S. Zinc finger proteins: getting a grip on RNA. *Curr Opin Struct Biol* **15**, 94-8 (2005).
15. Baxley, R.M. *et al.* Deciphering the DNA code for the function of the Drosophila polydactyl zinc finger protein Suppressor of Hairy-wing. *Nucleic Acids Res* **45**, 4463-4478 (2017).
16. Han, B.Y., Foo, C.S., Wu, S. & Cyster, J.G. The C2H2-ZF transcription factor Zfp335 recognizes two consensus motifs using separate zinc finger arrays. *Genes Dev* **30**, 1509-14 (2016).
17. Nakahashi, H. *et al.* A genome-wide map of CTCF multivalency redefines the CTCF code. *Cell Rep* **3**, 1678-1689 (2013).
18. Schmitges, F.W. *et al.* Multiparameter functional diversity of human C2H2 zinc finger proteins. *Genome Res* **26**, 1742-1752 (2016).
19. Imbeault, M., Helleboid, P.Y. & Trono, D. KRAB zinc-finger proteins contribute to the evolution of gene regulatory networks. *Nature* **543**, 550-554 (2017).
20. Persikov, A.V. & Singh, M. An expanded binding model for Cys2His2 zinc finger protein-DNA interfaces. *Phys Biol* **8**, 035010 (2011).
21. Breiman, L. Random Forests. *Machine Learning* **45**, 5-32 (2001).
22. Lam, K.N., van Bakel, H., Cote, A.G., van der Ven, A. & Hughes, T.R. Sequence specificity is obtained from the majority of modular C2H2 zinc-finger arrays. *Nucleic Acids Res* **39**, 4680-90 (2011).
23. Lambert, S.A., Albu, M., Hughes, T.R. & Najafabadi, H.S. Motif comparison based on similarity of binding affinity profiles. *Bioinformatics* **32**, 3504-3506 (2016).
24. Najafabadi, H.S., Albu, M. & Hughes, T.R. Identification of C2H2-ZF binding preferences from ChIP-seq data using RCADE. *Bioinformatics* **31**, 2879-81 (2015).
25. Jaganathan, K. *et al.* Predicting Splicing from Primary Sequence with Deep Learning. *Cell* **176**, 535-548 e24 (2019).
26. Pollard, K.S., Hubisz, M.J., Rosenbloom, K.R. & Siepel, A. Detection of nonneutral substitution rates on mammalian phylogenies. *Genome Res* **20**, 110-21 (2010).
27. Munro, D., Ghersi, D. & Singh, M. Two critical positions in zinc finger domains are heavily mutated in three human cancer types. *PLoS Comput Biol* **14**, e1006290 (2018).
28. Hoadley, K.A. *et al.* Cell-of-Origin Patterns Dominate the Molecular Classification of 10,000 Tumors from 33 Types of Cancer. *Cell* **173**, 291-304 e6 (2018).
29. Ignatiadis, N., Klaus, B., Zaugg, J.B. & Huber, W. Data-driven hypothesis weighting increases detection power in genome-scale multiple testing. *Nat Methods* **13**, 577-80 (2016).

30. Dogan, B. & Najafabadi, H.S. Computational Methods for Analysis of the DNA-Binding Preferences of Cys2His2 Zinc-Finger Proteins. *Methods Mol Biol* **1867**, 15-28 (2018).
31. Karolchik, D. *et al.* The UCSC Table Browser data retrieval tool. *Nucleic Acids Res* **32**, D493-6 (2004).
32. Yousef, A. & Charkari, N.M. A novel method based on physicochemical properties of amino acids and one class classification algorithm for disease gene identification. *J Biomed Inform* **56**, 300-6 (2015).
33. Hashimoto, H. *et al.* Structural Basis for the Versatile and Methylation-Dependent Binding of CTCF to DNA. *Mol Cell* **66**, 711-720 e3 (2017).
34. Zandarashvili, L., White, M.A., Esadze, A. & Iwahara, J. Structural impact of complete CpG methylation within target DNA on specific complex formation of the inducible transcription factor Egr-1. *FEBS Lett* **589**, 1748-53 (2015).
35. Case, D.A. *et al.* The Amber biomolecular simulation programs. *J Comput Chem* **26**, 1668-88 (2005).
36. Jorgensen, W.L., Chandrasekhar, J., Madura, J.D., Impey, R.W. & Klein, M.L. Comparison of simple potential functions for simulating liquid water. *The Journal of Chemical Physics* **79**, 926-935 (1983).
37. Galindo-Murillo, R., Bergonzo, C. & Cheatham III, T.E. Molecular Modeling of Nucleic Acid Structure. *Current Protocols in Nucleic Acid Chemistry* **54**, 7.5.1-7.5.13 (2013).
38. Essmann, U. *et al.* A smooth particle mesh Ewald method. *The Journal of Chemical Physics* **103**, 8577-8593 (1995).
39. Ryckaert, J.-P., Ciccotti, G. & Berendsen, H.J.C. Numerical integration of the cartesian equations of motion of a system with constraints: molecular dynamics of n-alkanes. *Journal of Computational Physics* **23**, 327-341 (1977).
40. Salomon-Ferrer, R., Götz, A.W., Poole, D., Le Grand, S. & Walker, R.C. Routine Microsecond Molecular Dynamics Simulations with AMBER on GPUs. 2. Explicit Solvent Particle Mesh Ewald. *Journal of Chemical Theory and Computation* **9**, 3878-3888 (2013).
41. Roe, D.R. & Cheatham, T.E. PTRAJ and CPPTRAJ: Software for Processing and Analysis of Molecular Dynamics Trajectory Data. *Journal of Chemical Theory and Computation* **9**, 3084-3095 (2013).
42. Kumar, P., Kailasam, S., Chakraborty, S. & Bansal, M. MolBridge: a program for identifying nonbonded interactions in small molecules and biomolecular structures. *Journal of Applied Crystallography* **47**, 1772-1776 (2014).
43. Schrodinger, LLC. The PyMOL Molecular Graphics System, Version 1.8. (2015).
44. Lek, M. *et al.* Analysis of protein-coding genetic variation in 60,706 humans. *Nature* **536**, 285-91 (2016).
45. Gao, J. *et al.* Integrative analysis of complex cancer genomics and clinical profiles using the cBioPortal. *Sci Signal* **6**, pl1 (2013).
46. Law, C.W., Chen, Y., Shi, W. & Smyth, G.K. voom: Precision weights unlock linear model analysis tools for RNA-seq read counts. *Genome Biol* **15**, R29 (2014).
47. Zhang, W. *et al.* A global transcriptional network connecting noncoding mutations to changes in tumor gene expression. *Nat Genet* **50**, 613-620 (2018).